Probing small-scale anisotropic inflation with stochastic gravitational wave background*

Yu-Ting Kuang (况宇庭)[1,2] Jing-Zhi Zhou (周敬之)[3] Zhe Chang (常哲)[1,2] Di Wu (吴迪)[4†]

[1]Institute of High Energy Physics, Chinese Academy of Sciences, Beijing 100049, China
[2]University of Chinese Academy of Sciences, Beijing 100049, China
[3]Center for Joint Quantum Studies and Department of Physics, School of Science, Tianjin University, Tianjin 300350, China
[4]School of Fundamental Physics and Mathematical Sciences, Hangzhou Institute for Advanced Study, UCAS, Hangzhou 310024, China

Abstract: In June 2023, multiple pulsar timing array (PTA) collaborations provided evidence for the existence of a stochastic gravitational wave background (SGWB). As a significant source of the SGWBs, scalar induced gravitational waves (SIGWs) receive extensive attention. We explore the influence of anisotropic primordial power spectra on second-order SIGWs and derive explicit expressions for the energy density spectra. For specific anisotropic inflation models, we analyze the impacts of Finslerian inflation and gauge field inflation models on PTA and Laser Interferometer Space Antenna (LISA) and generalize the findings to model-independent scenarios. Our results indicate that current PTA observations cannot rule out the existence of small-scale anisotropic primordial perturbations.

Keywords: scalar induced gravitational wave, stochastic gravitational wave background, inflation, pulsar timing array

DOI: **CSTR:**

I. INTRODUCTION

In June 2023, the pulsar timing array (PTA) collaborations NANOGrav [1], EPTA [2], PPTA [3], and CPTA [4] reported positive evidence for an isotropic, stochastic background of gravitational waves (GWs) within the nHz frequency range. The astrophysical origin of the stochastic gravitational wave background (SGWB) is primarily attributed to supermassive black hole binary (SMBHB) [5, 6]. Furthermore, the PTA observation has provided a new tool for probing new physics [7]. Various sources of SGWB have been investigated to explain the origin of current PTA observations. The cosmological explanations include cosmic strings and domain walls [8−10], cosmological phase transition gravitational waves [11, 12], and scalar induced gravitational waves (SIGWs) [13−19]. Ref. [7] analyzed the possibility that different sources of SGWB dominate current PTA observations. The results show that the SIGWs yield the highest Bayes factor, indicating that SIGWs are among the most likely sources of SGWB in PTA frequency band.

SIGWs originate from primordial curvature perturbations with large amplitudes on small scales. More precisely, large-scale cosmological observations such as cosmic microwave background (CMB) and large scale structure (LSS) have determined the amplitude of the power spectrum of primordial curvature perturbation to around 2×10^{-9} [20]. However, on small scales ($\lesssim$1 Mpc), current cosmological observations impose much weaker constraints on primordial curvature perturbations [21]. Large-amplitude primordial curvature perturbations on small scales can re-enter the horizon after inflation, thereby exciting higher-order SIGWs with significant observable effects. Since the second-order SIGWs are generated by primordial scalar perturbations for a specific inflation model, the parameter space of the inflation model can be constrained by current and future SGWB observations. Over the past two years, the SGWB in the PTA frequency band, dominated by SIGWs, has been systematically studied. Relevant research includes investigations into primordial non-Gaussianity [22−25], varying sound speed [15], different epochs of the Universe [26−28], and corrections from third-order SIGWs [14].

In current studies on SIGWs and PTA observations, it is common to assume a statistically isotropic primordial power spectrum on small scales, meaning that the spectrum $\mathcal{P}_\zeta(k)$ depends only on the magnitude of the wavenumber $\mathbf{k}$, and not on its direction. Given that present PTA data provide evidence for an isotropic SGWBs, this assumption of small-scale isotropy appears quite reasonable. However, it is important to emphasize

Received 30 October 2025; Accepted 3 February 2026

* The work is supported in part by the National Natural Science Foundation of China (NSFC) grants No.12475075, No.12447127

† E-mail: wudi@ucas.ac.cn

that this prior assumption is not mandatory. There exist strong physical motivations to explore primordial power spectra that exhibit anisotropy on small scales. As pointed out in Ref. [23, 29, 30], SIGWs originate from extremely high redshifts, corresponding to very small horizon scales. Due to the limited angular resolution of current detectors, the signal along any line of sight represents an ensemble average over many such horizon patches. Consequently, current PTA observations are incapable of resolving anisotropies in the primordial power spectrum at small scales. Constraining such anisotropic features remains an open question. In this paper, we investigate the second-order SIGWs generated by small-scale ($\lesssim$1 Mpc) statistically anisotropic primordial scalar perturbations. Models that can produce anisotropic primordial perturbations mainly fall into two categories: one involves introducing additional fields during inflation to generate anisotropy at the quantum level [31−35], and the other involves incorporating an anisotropic spacetime background, primarily focusing on Finslerian inflation [36−39]. Here, we investigate the impact of anisotropic primordial power spectra on SIGWs through a model-independent approach, specifically using a parametric method. When the primordial power spectrum exhibits anisotropy on small scales, the energy density spectra of second-order SIGWs are also anisotropic on small scales. Since the small-scale anisotropy of SIGWs cannot be observed by current PTA observations, we derive the isotropic energy density spectrum of SIGWs in terms of spatially averaging the anisotropic SIGWs on small scales. We find that the spatial averaging does not eliminate the influence of the anisotropic parameters. The potential small-scale anisotropic primordial power spectra can be constrained by current PTA observations of the isotropic energy density spectrum of SIGWs.

The remainder of this paper is organized as follows. In Sec. II we review the calculations of the second-order SIGWs. In Sec. III, we calculate the second-order SIGWs for cases of anisotropic primordial power spectra. In Sec. IV, we present several models of anisotropic primordial power spectra and use PTA+CMB+baryon acoustic oscillations (BAO) data to constrain the anisotropy parameters. We summarize our results in Sec. V.

II. REVIEW OF SCALAR INDUCED GRAVITATIONAL WAVE

When studying SIGWs, the effects of primordial vector and tensor perturbations are typically ignored. Primordial vector perturbations, in particular, decay as a^{-2}, making their contribution negligible [40]. Although primordial tensor perturbations are well-constrained on large scales, their amplitude can be enhanced at small scales using specific inflationary models [41−43]. In such scenarios, primordial tensor perturbations could have a significant impact on the induced GWs [44]. In this paper, we focus solely on the large primordial scalar perturbations on small scales. The perturbed metric in the Friedmann-Lemaitre-Robertson-Walker (FLRW) spacetime with Newtonian gauge can be written as

$$\mathrm{d}s^2 = a^2\left(-\left(1+2\phi^{(1)}\right)\mathrm{d}\eta^2 + \left(\left(1-2\psi^{(1)}\right)\delta_{ij} + \frac{1}{2}h_{ij}^{(2)}\right)\mathrm{d}x^i\mathrm{d}x^j\right), \tag{1}$$

where $\phi^{(1)}$ and $\psi^{(1)}$ are the first-order scalar perturbations. $h_{ij}^{(2)}$ is the second-order tensor perturbation. In this paper, we study SIGWs generated during the radiation-dominated (RD) era ($\omega = 1/3$ and $c_s = 1/\sqrt{3}$). The equations of motion of first-order scalar perturbations are given by

$$\begin{aligned} &6\psi^{(1)\prime\prime}(\mathbf{x},\eta) + \Delta(3\phi^{(1)}(\mathbf{x},\eta) - 5\psi^{(1)}(\mathbf{x},\eta)) \\ &\quad + 6\mathcal{H}(\phi^{(1)\prime}(\mathbf{x},\eta) + 3\psi^{(1)\prime}(\mathbf{x},\eta)) = 0\,, \\ &\psi^{(1)}(\mathbf{x},\eta) - \phi^{(1)}(\mathbf{x},\eta) = 0\,, \end{aligned} \tag{2}$$

where, the prime stands for the derivative with respect to the conformal time η, and the $\mathcal{H} = aH = 1/\eta$ is conformal Hubble parameter. In momentum space, the solutions of Eq. (2) can be written as [45]

$$\begin{aligned} \psi^{(1)}(\mathbf{k},\eta) &= \phi^{(1)}(\mathbf{k},\eta) = T_\phi(k\eta)\phi_{\mathbf{k}} \\ &= \frac{9}{(k\eta)^2}\left(\frac{\sin(k\eta/\sqrt{3})}{k\eta/\sqrt{3}} - \cos(k\eta/\sqrt{3})\right)\frac{2}{3}\zeta_{\mathbf{k}}\,, \end{aligned} \tag{3}$$

in which, $T_\phi(x)$ is the transfer function of $\phi^{(1)}$, and $\zeta_{\mathbf{k}}$ represents the primordial curvature perturbation. We have set $k = |\mathbf{k}|$ in Eq. (3).

By expanding the Einstein field equations to second-order, we obtain the equation of motion of second-order SIGWs

$$h_{ij}^{(2)\prime\prime}(\mathbf{x},\eta) + 2\mathcal{H}h_{ij}^{(2)\prime}(\mathbf{x},\eta) - \Delta h_{ij}^{(2)}(\mathbf{x},\eta) = -4S_{ij}^{(2)}(\mathbf{x},\eta)\,, \tag{4}$$

where the source term $S_{ij}^{(2)}(\mathbf{x},\eta)$ is given by

$$\begin{aligned} S_{ij}^{(2)}(\mathbf{x},\eta) = \Lambda_{ij}^{rs}\Big(&3\phi^{(1)}\partial_r\partial_s\phi^{(1)} + \frac{2}{\mathcal{H}}\phi^{(1)\prime}\partial_r\partial_s\phi^{(1)} \\ &+ \frac{1}{\mathcal{H}^2}\phi^{(1)\prime}\partial_r\partial_s\phi^{(1)\prime}\Big)\,. \end{aligned} \tag{5}$$

We have simplified the above equation using the relation $\Lambda_{ij}^{rs}\partial_r\phi\partial_s\phi = -\Lambda_{ij}^{rs}\phi\partial_r\partial_s\phi$, where

$$\Lambda_{ij}^{rs} = \mathcal{T}_i^r\mathcal{T}_j^s - \frac{1}{2}\mathcal{T}_{ij}\mathcal{T}^{rs} \tag{6}$$

is the transverse and traceless operator, where $\mathcal{T}_{ij}=\delta_{ij}-\partial_i\Delta^{-1}\partial_j$ is the traceless operator. By taking the Fourier transform of Eq. (4), we obtain

$$h_{\mathbf{k}}^{\lambda,(2)\prime\prime}(\eta)+2\mathcal{H}h_{\mathbf{k}}^{\lambda,(2)\prime}(\eta)+k^2h_{\mathbf{k}}^{\lambda,(2)}(\eta)=-4S_{\mathbf{k}}^{\lambda,(2)}(\eta)\,, \quad (7)$$

where the source term $S_{\mathbf{k}}^{\lambda,(2)}(\eta)$ is given by

$$S_{\mathbf{k}}^{\lambda,(2)}(\eta)=-\int\frac{\mathrm{d}^3\mathbf{p}}{(2\pi)^{3/2}}e^{\lambda,ij}(\mathbf{k})p_ip_j\Big(2\phi_{\mathbf{p}}\phi_{\mathbf{k}-\mathbf{p}}+(\mathcal{H}^{-1}\phi_{\mathbf{p}}'+\phi_{\mathbf{p}})(\mathcal{H}^{-1}\phi_{\mathbf{k}-\mathbf{p}}'+\phi_{\mathbf{k}-\mathbf{p}})\Big)\,. \quad (8)$$

In Eq. (8), $e^{\lambda,ij}(\mathbf{k})$ represents the polarization tensor. The energy density spectrum of second-order SIGWs can be calculated using the following formula:

$$\Omega_{\mathrm{GW}}(k,\eta)=\frac{\rho_{\mathrm{GW}}(k,\eta)}{\rho_{\mathrm{tot}}(\eta)}=\frac{1}{24}\left(\frac{k}{\mathcal{H}}\right)^2\mathcal{P}_h(k,\eta)\,, \quad (9)$$

where $\mathcal{P}_h(k,\eta)$ represents the power spectrum of second-order SIGWs, which is defined as

$$\left\langle h_{\mathbf{k}}^{\lambda,(2)}(\eta)h_{\mathbf{k}'}^{\lambda',(2)}(\eta)\right\rangle=\delta^{\lambda\lambda'}\delta^3(\mathbf{k}+\mathbf{k}')\frac{2\pi^2}{k^3}\mathcal{P}_h^{(2)}(k,\eta)\,. \quad (10)$$

As shown in Ref. [46], the power spectrum of second-order SIGWs $\mathcal{P}_h^{(2)}(k,\eta)$ is given by

$$\mathcal{P}_h^{(2)}(k,\eta)=4\int_0^\infty\mathrm{d}v\int_{|1-v|}^{1+v}\mathrm{d}u\left(\frac{4v^2-(1+v^2-u^2)^2}{4uv}\right)^2\times(I(v,u,x))^2\mathcal{P}_\zeta(kv)\mathcal{P}_\zeta(ku)\,, \quad (11)$$

where $\mathcal{P}_\zeta(k)$ is the power spectrum of primordial curvature perturbation. We have defined $x=k\eta$, $u=|\mathbf{k}-\mathbf{p}|/k$ and $v=p/k$. The expression for the kernel function $I(v,u,x)$ is given by

$$I(u,v,x)=\frac{4}{k^2}\int_0^x\mathrm{d}\bar{x}\left(\frac{\bar{x}}{x}\sin(x-\bar{x})f(u,v,\bar{x})\right)\,, \quad (12)$$

where the function $f(v,u,x)$, derived from the source term in Eq. (8), can be expressed as

$$\begin{aligned}f(v,u,x)=\frac{12}{u^3v^3x^6}\Bigg(&18uvx^2\cos\frac{ux}{\sqrt{3}}\cos\frac{vx}{\sqrt{3}}\\&+(54-6(u^2+v^2)x^2+u^2v^2x^4)\sin\frac{ux}{\sqrt{3}}\sin\frac{vx}{\sqrt{3}}\\&+2\sqrt{3}ux(v^2x^2-9)\cos\frac{ux}{\sqrt{3}}\sin\frac{vx}{\sqrt{3}}\\&+2\sqrt{3}vu(u^2x^2-9)\sin\frac{ux}{\sqrt{3}}\cos\frac{vx}{\sqrt{3}}\Bigg)\,.\end{aligned} \quad (13)$$

By evaluating the integral in Eq. (12), we obtain the analytical expression for the kernel function $I(u,v,x)$ as [46]

$$\begin{aligned}k^2I(u,v,x\to\infty)=&\frac{27(u^2+v^2-3)}{u^3v^3x}\\&\times\Bigg(\sin x\Big(-4uv+(u^2+v^2-3)\\&\times\ln\left|\frac{3-(u+v)^2}{3-(u-v)^2}\right|\Big)\\&-\pi(u^2+v^2-3)\Theta(v+u-\sqrt{3})\cos x\Bigg)\,,\end{aligned} \quad (14)$$

where we have used the following approximations: $\lim_{x\to\pm\infty}\mathrm{Si}(x)=\pm\pi/2$ and $\lim_{x\to\infty}\mathrm{Ci}(x)=0$ in Eq. (14). Using the analytical expression of the kernel function given in Eq. (14), together with the results for the corresponding power spectrum and the energy density spectrum provided in Eq. (11) and Eq. (9), we obtain the formula for the energy density spectrum of second-order SIGWs during the RD era:

$$\begin{aligned}\Omega_{\mathrm{GW}}(k)=&\int_0^\infty\mathrm{d}v\int_{|1-v|}^{1+v}\mathrm{d}u\mathcal{P}_\zeta(uk)\mathcal{P}_\zeta(vk)\\&\times\frac{3}{1024u^8v^8}(u^2+v^2-3)^2\left[4v^2-(1+v^2-u^2)^2\right]^2\\&\times\left\{\left[(u^2+v^2-3)\ln\left|\frac{3-(u+v)^2}{3-(u-v)^2}\right|-4uv\right]^2\right.\\&\left.+\pi^2(u^2+v^2-3)^2\Theta\left(u+v-\sqrt{3}\right)\right\}\,,\end{aligned} \quad (15)$$

where we have performed an oscillatory average of the squared kernel function using the relations $\sin^2x\sim1/2$ and $\cos^2x\sim1/2$ [47]. Given a specific form of the power spectrum of primordial curvature perturbation $\mathcal{P}_\zeta(k)$, we can use Eq. (15) to calculate the energy density spectrum of second-order SIGWs during the RD era.

III. ANISOTROPIC PRIMORDIAL POWER SPECTRUM AND SIGWs

A. Energy density spectrum

To induce anisotropy in primordial curvature perturbations, one primary approach is to introduce an anisotropic vector field during the inflationary period. Through coupling between the vector field and the inflaton field [31−35, 48], the power spectrum of primordial curvature perturbation becomes anisotropic. Another key approach is to modify the background spacetime during inflation to the Finsler spacetime [36−39], leading to anisotropic

primordial curvature perturbations through calculations similar to those in traditional inflation models.

In this paper, we adopt a model-independent approach by studying the anisotropic primordial power spectrum through parameterization. We express the small-scale anisotropic primordial power spectrum as follows

$$\mathcal{P}_\zeta^{\hat{\mathbf{n}}}(\mathbf{k}) = \mathcal{P}_{0,\zeta}(k)\sum_{l=0}^{\infty}(-i)^l(2l+1)A_l(k)\mathcal{P}_l(\hat{\mathbf{n}}\cdot\hat{\mathbf{k}})\,, \tag{16}$$

where $\hat{\mathbf{n}}$ is the direction of the anisotropy, $\hat{\mathbf{k}}$ is the unit vector along $\mathbf{k}$ and $\mathcal{P}_l$ is the Legendre polynomial of order l. When $A_0(k)=1$ and $A_l(k)=0$ for $l\geq 1$, the primordial power spectrum reduces to $\mathcal{P}_{0,\zeta}(k)$, corresponding to the isotropic case. Previous studies have investigated the cases where A_0 and A_2 are non-zero [49]. In this paper, we consider the anisotropic primordial power spectrum with $A_l\neq 0$ for $l\leq 4$. In this case, Eq. (16) can be rewritten as

$$\mathcal{P}_\zeta^{\hat{\mathbf{n}}}(\mathbf{k}) = \mathcal{P}_{0,\zeta}(k)\sum_{l=0}^{4}C_l(k)\mathcal{P}_l(\hat{\mathbf{n}}\cdot\hat{\mathbf{k}})\,, \tag{17}$$

where $C_l=(-i)^l(2l+1)A_l(k)$. For simplicity, in the following discussion, we will neglect the dependence of C_l on k, assuming that C_l is constant on small scales.

Since the current angular resolution of GW observations cannot detect small-scale anisotropies, we need to perform spatial averaging of the anisotropic power spectrum to obtain an isotropic energy density spectrum. After spatial averaging, the power spectrum of the second-order GWs induced by anisotropic primordial scalar perturbations can be expressed as

$$\begin{aligned}\mathcal{P}_h^{(2)}(k,\eta) = 4\int_0^{2\pi}\mathrm{d}\phi_n\int_0^{\pi}\frac{\sin(\theta_n)}{4\pi}\mathrm{d}\theta_n\int_0^{2\pi}\frac{\mathrm{d}\phi_p}{2\pi}\int_0^{\infty}\mathrm{d}v\int_{|1-v|}^{1+v}\mathrm{d}u\left(\mathcal{P}_{0,\zeta}(kv)\sum_{l_1=0}^{4}C_{l_1}\mathcal{P}_{l_1}(\hat{\mathbf{n}}\cdot\hat{\mathbf{p}})\right)\\ \left(\mathcal{P}_{0,\zeta}(ku)\sum_{l_2=0}^{4}C_{l_2}\mathcal{P}_{l_2}(\hat{\mathbf{n}}\cdot\widehat{\mathbf{k}-\mathbf{p}})\right)\left(\frac{4v^2-(1+v^2-u^2)^2}{4uv}\right)^2 I^2(v,u,x)\,,\end{aligned} \tag{18}$$

where ϕ_n and θ_n are the azimuth and elevation of $\hat{\mathbf{n}}$, and ϕ_p is the azimuth of $\hat{\mathbf{p}}$. For convenience, we introduce

$$Q_{l_1,l_2} = \int_0^{2\pi}\mathrm{d}\phi_n\int_0^{\pi}\sin(\theta_n)\mathrm{d}\theta_n\mathcal{P}_{l_1}(\hat{\mathbf{n}}\cdot\hat{\mathbf{p}})\mathcal{P}_{l_2}(\hat{\mathbf{n}}\cdot\widehat{\mathbf{k}-\mathbf{p}})\,, \tag{19}$$

which allows Eq. (18) to be rewritten as

$$\mathcal{P}_h^{(2)}(k,\eta) = 4\int_0^{\infty}\mathrm{d}v\int_{|1-v|}^{1+v}\mathrm{d}u\left(\frac{4v^2-(1+v^2-u^2)^2}{4uv}\right)^2\left(\sum_{l_1,l_2=0}^{4}C_{l_1}C_{l_2}Q_{l_1,l_2}\right)\times(I(v,u,x))^2\mathcal{P}_{0,\zeta}(kv)\mathcal{P}_{0,\zeta}(ku)\,. \tag{20}$$

By comparing Eq. (11) with Eq. (20), we find that the impact of the anisotropic power spectrum is only reflected in the additional terms in the first line of Eq. (20). The analytical result of Q_{l_1,l_2} in Eq. (19) and Eq. (20) is given by

$$\begin{aligned}Q_{0,0} &= 4\pi\,,\\ Q_{1,1} &= -2\pi\frac{u^2+v^2-1}{3uv}\,,\\ Q_{2,2} &= \pi\frac{3u^2+2u^2(v^2-3)+3(v^2-1)^2}{10u^2v^2}\,,\\ Q_{3,3} &= -\pi(u^2+v^2-1)\frac{5(u^2-1)^2+5v^4-2v^2(u^2+5)}{28u^3v^3}\\ Q_{4,4} &= \pi\Big(35u^8+20u^4(v^2-7)+20u^2(v^2-1)^2(v^2-7)\\ &\quad +35(v^2-1)^4+6u^4(3v^4-30v^2+35)\Big)\frac{1}{288u^4v^4}\,,\\ Q_{l_1,l_2} &= 0\quad (l_1\neq l_2)\,.\end{aligned} \tag{21}$$

By substituting Eq. (20) into Eq. (9), we obtain the corresponding expression for the energy density spectrum during the RD era:

$$\Omega_{\rm GW}(k)=\int_0^\infty {\rm d}v\int_{|1-v|}^{1+v}{\rm d}u\mathcal{P}_\zeta(uk)\mathcal{P}_\zeta(vk)\left(\sum_{l_1,l_2=0}^{4}C_{l_1}C_{l_2}Q_{l_1,l_2}\right)\times\frac{3}{1024u^8v^8}(u^2+v^2-3)^2\left[4v^2-(1+v^2-u^2)^2\right]^2$$
$$\times\left\{\left[(u^2+v^2-3)\ln\left|\frac{3-(u+v)^2}{3-(u-v)^2}\right|-4uv\right]^2+\pi^2(u^2+v^2-3)^2\Theta\left(u+v-\sqrt{3}\right)\right\}\ . \tag{22}$$

When considering the small-scale anisotropic primordial power spectrum for $l\le 4$, the corresponding energy density spectrum of second-order SIGWs can be directly computed using Eq. (22). As previously discussed, current observations of the SGWB are unable to resolve the anisotropies generated by the small-scale anisotropic primordial power spectrum. As shown in Eq. (22), even after taking the spatial average of the energy density spectrum of SIGWs, the anisotropy parameters C_l still affect the energy density spectrum. Therefore, the observations of the current SGWB can be used to constrain the small-scale anisotropic primordial power spectrum.

B. Anisotropy of SIGWs

In the previous subsection, we derived the explicit expression for the energy density spectrum of second-order SIGWs after performing spatial averaging, which originates from the small-scale anisotropic primordial power spectrum. As we mentioned earlier, due to the limited precision of current observational data, such small-scale anisotropies cannot be directly detected. Nevertheless, analyzing the anisotropy of the energy density spectrum of SIGWs at small scales remains meaningful, as it may provide a window for probing small-scale anisotropic inflationary models in the future. In this subsection, we compute the anisotropy of second-order SIGWs at small scales. For simplicity, we focus on the primordial power spectrum with $l=0$ and $l=2$. Such an anisotropic primordial spectrum is typically associated with anisotropic inflationary models involving vector fields or gauge fields, which will be discussed in Sec. IV. Based on Eq. (16), the anisotropic primordial power spectrum in this scenario can be expressed as

$$\mathcal{P}_\zeta^{\hat{\mathbf{n}}}(\mathbf{k})=\mathcal{P}_{0,\zeta}(k)\left(1-5A_2(k)\right)\mathcal{P}_l(\hat{\mathbf{n}}\cdot\hat{\mathbf{k}})\ . \tag{23}$$

By substituting Eq. (23) into Eq. (11) and simplifying, we obtain [49]

$$\Omega_{\rm GW}^{\mathbf{n}}(\eta,\mathbf{k})=\sum_{l=0}^{\infty}(-i)^l(2l+1)\Omega_l(\eta,k)P_l(\hat{\mathbf{n}}\cdot\hat{\mathbf{k}})\ . \tag{24}$$

In Eq. (24), $\Omega_l(\eta,k)$ represents the multipole moment associated with second-order SIGWs, and its explicit form can be expressed as

$$\Omega_l(x,k)=\frac{x^2}{6}\int_0^\infty {\rm d}v\int_{|1-v|}^{1+v}{\rm d}u\left(\frac{4v^2-(1+v^2-u^2)^2}{4uv}\right)^2 I^2(u,v,x)\mathcal{P}_\zeta(uk)\mathcal{P}_\zeta(vk)\left[\delta_{l0}+H_l(u,v,x)\right]\ , \tag{25}$$

where δ_{l0} is the Kronecker delta. And H_l in Eq. (25) are given by

$$H_0=\ A_2(uk)A_2(vk)\frac{160}{81u^2v^2}\left(3u^4+2u^2(v^2-3)+3(v^2-1)^2\right)\ , \tag{26}$$

$$H_2=\frac{32A_2(uk)}{81u^2v^2}\left(3u^4v^2+2u^2v^2(1-3v^2)+3v^2(v^2-1)^2\right)+\frac{32A_2(vk)}{81u^2v^2}\left(3u^2(1+v^2-u^2)^2-4u^2v^2\right)$$
$$-\frac{160A_2(uk)A_2(vk)}{567}\frac{1}{u^2v^2}\left(3u^6-3u^4(v^2+1)+3(v^2-1)^2(v^2+1)-u^2(3+2v^2+3v^4)\right)\ , \tag{27}$$

$$H_4=\frac{20A_2(uk)A_2(vk)}{567u^2v^2}\Big(35u^8-20u^6(3+7v^2)+6u^4(3+10v^2+35v^4)$$
$$+4u^2(1+3v^2+15v^4-35v^6)+(v^2-1)^2(3+10v^2+35v^4)\Big)\ . \tag{28}$$

To better illustrate the small-scale anisotropy of second-order SIGWs, we consider the following form of the monochromatic primordial power spectrum

$$\mathcal{P}_{0,\zeta}(k) = A_\zeta k_* \delta(k - k_*) \,. \tag{29}$$

In this scenario, the multipole moment of the energy density spectrum of second-order SIGWs in Eq. (25) is given by

$$\Omega_l^\delta(\tilde{k}) = \Omega_{\rm iso}^\delta(\tilde{k}) \left(\delta_{l0} + H_l^\delta(\tilde{k})\right) \,, \tag{30}$$

where

$$\begin{aligned}\Omega_{\rm iso}^\delta(\tilde{k}) = {} & \frac{3A_\zeta^2}{64}\left(\frac{\tilde{k}^2-4}{4}\right)^2 \tilde{k}^2(3\tilde{k}^2-2)^2 \\ & \times \left(\pi^2(3\tilde{k}^2-2)^2\,\Theta\left(\frac{2}{\sqrt{3}}-\tilde{k}\right)\right. \\ & \left. + \left(4+(3\tilde{k}^2-2)\ln\left|1-\frac{4}{3\tilde{k}^2}\right|^2\right)\Theta(2-\tilde{k})\right) \,,\end{aligned} \tag{31}$$

$$H_0^\delta(\tilde{k}) = \frac{5A_2^2}{8}\left(8-12\tilde{k}^2+3\tilde{k}^4\right) \,, \tag{32}$$

$$H_2^\delta(\tilde{k}) = \frac{A_2}{4}(3\tilde{k}^2-4) + \frac{5A_2^2}{56}(8+6\tilde{k}^2-3\tilde{k}^4) \,, \tag{33}$$

$$H_4^\delta(\tilde{k}) = \frac{5A_2^2}{448}(48+8\tilde{k}^2+3\tilde{k}^4) \,. \tag{34}$$

In Fig. 1, we present the results for the multipole moments of the energy density spectrum of second-order scalar-induced gravitational waves, obtained under the assumption of a monochromatic primordial power spectrum in Eq. (23) and Eq. (29).

IV. DETECTION OF ANISOTROPIC PRIMORDIAL POWER SPECTRUM

To calculate the power spectrum of the second-order SIGWs, we need to provide the specific expression of the primordial power spectrum. In this paper, we consider the log-normal primordial power spectrum [50–53]

$$\mathcal{P}_{0,\zeta}(k) = \frac{A_\zeta}{\sqrt{2\pi\sigma^2}} \exp\left(-\frac{\ln^2(k/k_*)}{2\sigma^2}\right) \,, \tag{35}$$

where A_ζ is the amplitude of the primordial power spectrum, $k_* = 2\pi f_*$ is the wavenumber at which the power spectrum has a log-normal peak, and σ characterizes the width of the log-normal distribution. The anisotropy of the primordial power spectrum on small scales is characterized by the parameters C_l ($l = 1,2,3,4$) in Eq. (17). The energy density of second-order SIGW during the RD era can be calculated in terms of Eq. (22). Taking into account the thermal history of the universe, we obtain the current total energy density spectrum of SIGWs [54]

$$\Omega_{0,\rm GW}(k) = \Omega_{rad,0}\left(\frac{g_{*,\rho,e}}{g_{*,\rho,0}}\right)\left(\frac{g_{*,s,0}}{g_{*,s,e}}\right)^{4/3} \Omega_{\rm GW}(k,\eta) \,, \tag{36}$$

where $\Omega_{rad,0} = 4.2\times10^{-5}h^{-2}$ is the energy density fraction of radiation today, and the dimensionless Hubble constant is $h = 0.6736$ [20]. The $g_{*,\rho}$ and $g_{*,s}$ are the effective numbers of relativistic degrees of freedom [55]. In Fig. 2,

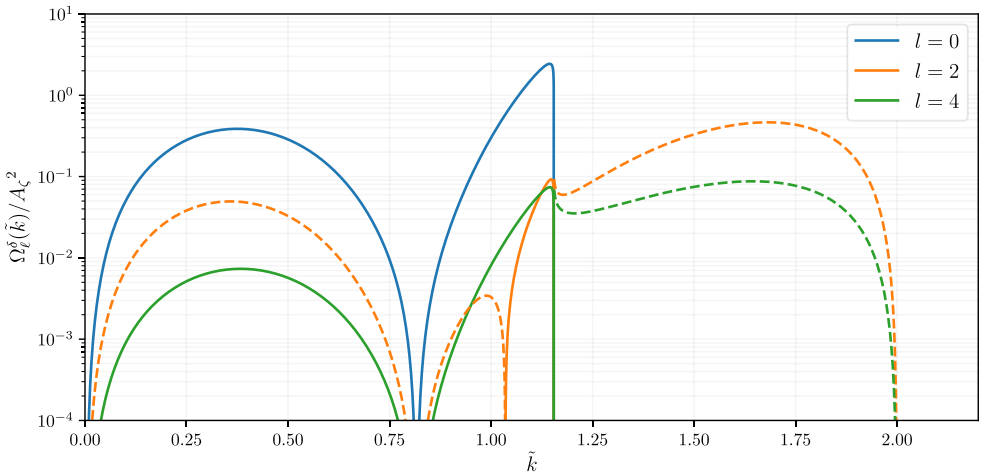

Fig. 1. (color online) Ω_l^δ as a function of $\tilde{k}$, assuming $A_2 = 0.2$. The dashed curves denote the absolute value of the negative ratios of $l = 0, 2$.

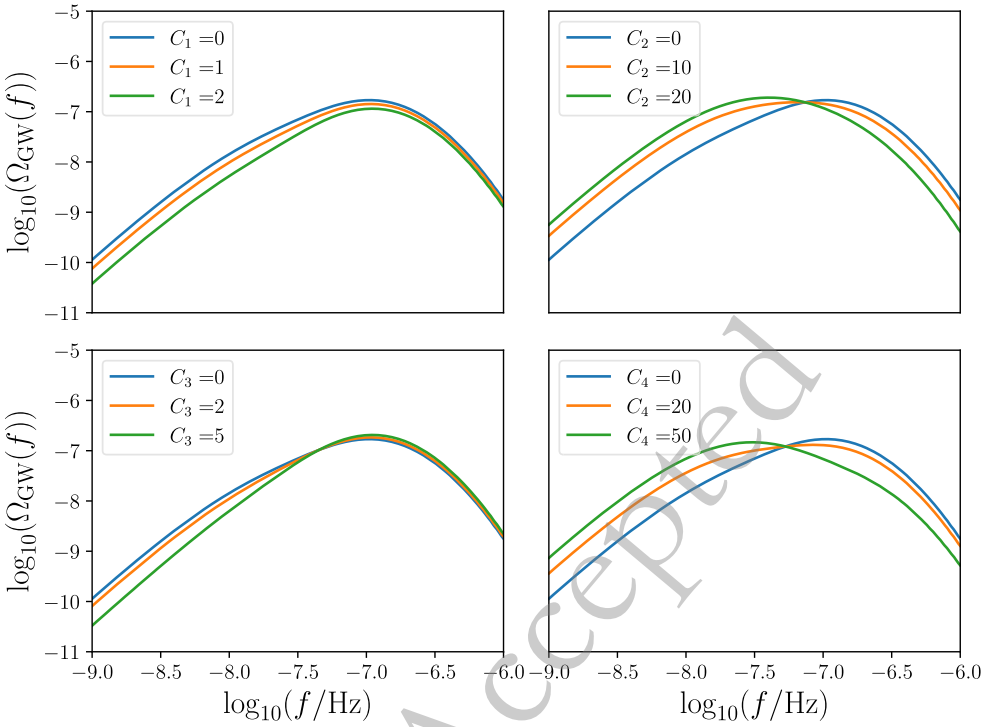

Fig. 2. (color online) The impact of different C_l parameters on the energy density spectrum is shown. Here, f_*, A_ζ, and σ are fixed at 10^{-7} Hz, 0.5, and 1, respectively. In each subplot, only C_1, C_2, C_3, or C_4 is non-zero, from left to right. Different colors in the figure represent different values of the C_l parameter, as indicated in the legend.

we illustrate the impact of different C_l ($l=1,2,3,4$) parameters on the energy density spectrum of second-order SIGWs under a log-normal primordial power spectrum. In this paper, we consider the following two types of anisotropic inflation models:

1, Gauge field: Introducing a vector (gauge) field during inflation can serve as a mechanism for generating cosmic anisotropy. In this type of model, the primordial power spectrum can be parameterized as follows [56]

$$\mathcal{P}_\zeta^{\hat{\mathbf{n}}}(\mathbf{k}) = \mathcal{P}_{0,\zeta}(k)\left(1+C_2\mathcal{P}_2(\hat{\mathbf{n}}\cdot\hat{\mathbf{k}})\right) . \tag{37}$$

2, Finslerian inflation: Modifying the spacetime background during inflation can introduce anisotropy. One of the most prominent spacetime backgrounds for this purpose is the Finsler spacetime background. In this model, the form of the anisotropic primordial power spectrum is given by [57]

$$\mathcal{P}_\zeta^{\hat{\mathbf{n}}}(\mathbf{k}) = \mathcal{P}_{0,\zeta}(k)\left(1+C_1\mathcal{P}_1(\hat{\mathbf{n}}\cdot\hat{\mathbf{k}})\right) . \tag{38}$$

The aforementioned two inflation models have presented the anisotropic primordial power spectra under the conditions of $C_2\neq 0$ and $C_1\neq 0$, respectively. In the rest of this section, we will discuss the impact of these two models on PTA and LISA observations separately, and consider model-independent scenarios where both C_1 and C_2 are non-zero.

A. PTA observations and large-scale cosmological constraints

To constrain the parameter space of the anisotropic primordial power spectrum using PTA observations, we employ the kernel density estimator (KDE) representations of the free spectra to construct the likelihood function [58−60]

$$\ln\mathcal{L}(d|\theta) = \sum_{i=1}^{N_f} p(\Phi_i,\theta) . \tag{39}$$

In Eq. (39), $p(\Phi_i,\theta)$ represents the probability density of Φ_i given the parameter θ, and $\Phi_i=\Phi(f_i)$ denotes the time delay

$$\Phi(f) = \sqrt{\frac{H_0^2\Omega_{\rm GW}(f)}{8\pi^2 f^5 T_{\rm obs}}} , \tag{40}$$

where $H_0 = h\times 100$km/s/Mpc is the present-day value of the Hubble constant. Specifically, we directly utilize the publicly available KDE representations of the free spectrum provided by the NANOGrav 15-year dataset [61]. These KDEs are constructed from the analysis that expli-

citly accounts for Hellings-Downs spatial correlations. By adopting these official HD-correlated KDEs, our analysis strictly preserves the spatial information inherent in the PTA data, ensuring that the constraints are derived from a signal consistent with a gravitational wave background rather than uncorrelated common red noise. The Bayesian analysis is performed via BILBY [62] using its integrated DYNESTY nested sampler [63, 64]. For the anisotropic primordial power spectra, the posterior distributions are presented in Fig. 3–Fig. 5, with prior distributions for $\log_{10}(f_*/\mathrm{Hz})$, $\log_{10}(A_\zeta)$, σ, $\log_{10}(C_1)$ and $\log_{10}(C_2)$ set as uniform over the intervals $[-10,-5]$, $[-4,0]$, $[0.1,10]$, $[-3,1]$, and $[-2,3]$, respectively. Here, we have set $C_l = 0$ $(l > 2)$. The corresponding energy density spectra of second-order SIGWs are given in Fig. 6. As illustrated in Fig. 3–Fig. 5, PTA observations are able to effectively constrain the parameters A_ζ, σ, and f_* that characterize the isotropic primordial power spectrum. However, due to the presence of parameter degeneracies, the current PTA data fail to provide effective constraints on the parameters C_1 and C_2 that describe small-scale anisotropies. There are two main reasons for this result. First, the current PTA observational data are not sufficiently precise. Second, the introduction of the anisotropy parameter C_l leads to increased degeneracy in the energy density spectrum of SIGWs. To better constrain the primordial power spectrum anisotropies on small scales, it is necessary to consider additional cosmological observations that can place limits on the energy density spectrum of SIGWs.

In this section, we consider the constraints from large-scale cosmological observations on second-order SIGWs and the corresponding parameter space of the small-scale anisotropic primordial power spectrum. Large-scale cosmological observations constrain the SGWB via two kinds of methods. The first treats the SGWB as an additional radiation component, modifying the effective number of relativistic species, $N_{\rm eff}$. To remain consistent with current observational bounds, the total energy density spectrum must satisfy [65, 66]

$$\int_{f_{\rm min}}^{\infty} h^2\Omega_{\rm GW,0}(k)\mathrm{d}(\ln k) < 1.3\times10^{-6}\frac{\Delta N_{\rm eff}}{0.234}\,, \tag{41}$$

where $\Delta N_{\rm eff} = N_{\rm eff} - 3.046$. Here, we use the $N_{\rm eff}$ limits provided by [20], which report $N_{\rm eff} = 3.04 \pm 0.22$ at a 95% confidence level for the Planck + BAO + Big-Bang nucleosynthesis (BBN) data. The second method directly utilizes CMB and BAO measurements, imposing the following stricter constraint

$$\int_{f_{\rm min}}^{\infty} h^2\Omega_{\rm GW,0}(k)\mathrm{d}(\ln k) < 2.9\times10^{-7}\,, \tag{42}$$

at 95% confidence level for CMB+BAO data [67]. As shown in Fig. 7–Fig. 9, we present the current constraints

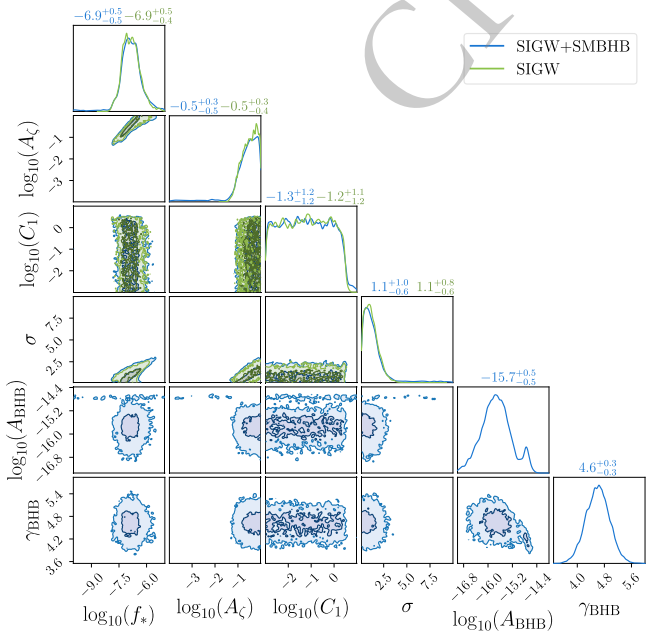

Fig. 3. (color online) Corner plot showing the posterior distributions with $C_1 \neq 0$. The blue and green curves correspond to the NANOGrav 15-year dataset. Off-diagonal panels display 1-σ and 2-σ confidence intervals for joint distributions, while diagonal panels provide marginal distributions with median values and 1-σ uncertainties noted above each histogram.

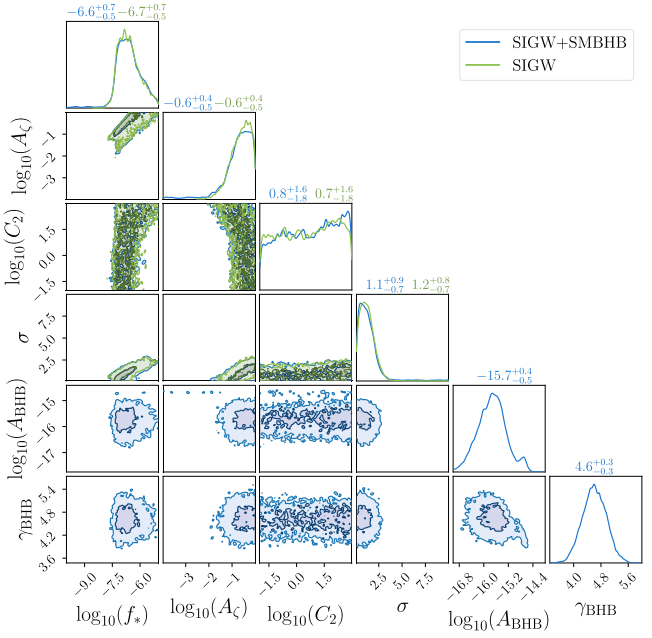

Fig. 4. (color online) Corner plot showing the posterior distributions with $C_2 \neq 0$. The blue and green curves correspond to the NANOGrav 15-year dataset. Off-diagonal panels display 1-σ and 2-σ confidence intervals for joint distributions, while diagonal panels provide marginal distributions with median values and 1-σ uncertainties noted above each histogram.

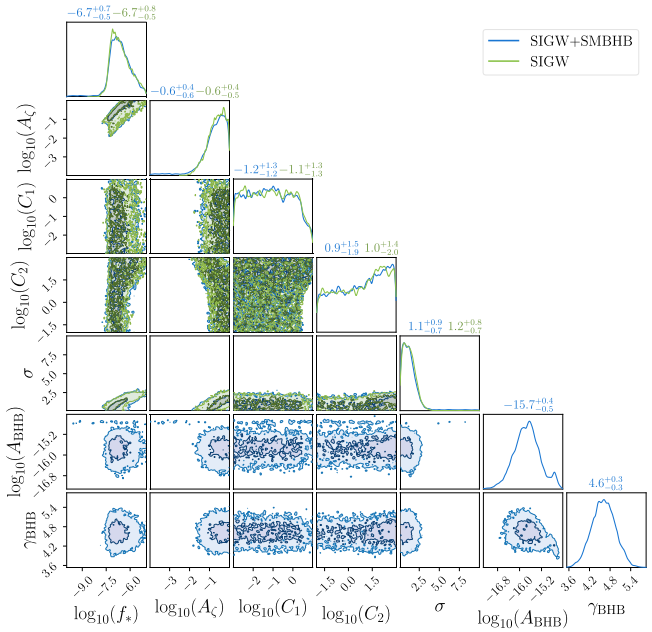

Fig. 5. (color online) Corner plot showing the posterior distributions with $C_l \neq 0$ $(l = 1, 2)$. The blue and green curves correspond to the NANOGrav 15-year dataset. Off-diagonal panels display 1-σ and 2-σ confidence intervals for joint distributions, while diagonal panels provide marginal distributions with median values and 1-σ uncertainties noted above each histogram.

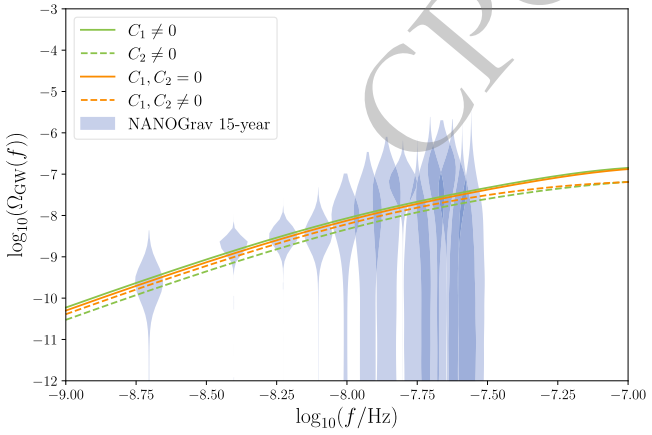

Fig. 6. (color online) The energy density spectra of second-order SIGWs with anisotropic primordial power spectra. The curves are based on parameters derived from the median values of the posterior distributions of the NANOGrav 15-year dataset. The energy density spectra derived from the free spectrum of the NANOGrav 15-year dataset is shown with blue shading. Different line styles and colors indicate scenarios with $C_1, C_2 = 0$, $C_1 \neq 0$, $C_2 \neq 0$, and $C_1, C_2 \neq 0$, as labeled in the figure.

from large-scale cosmological observations on the parameter space composed of C_1 and C_2, where the green line and the red line correspond to the observational limits

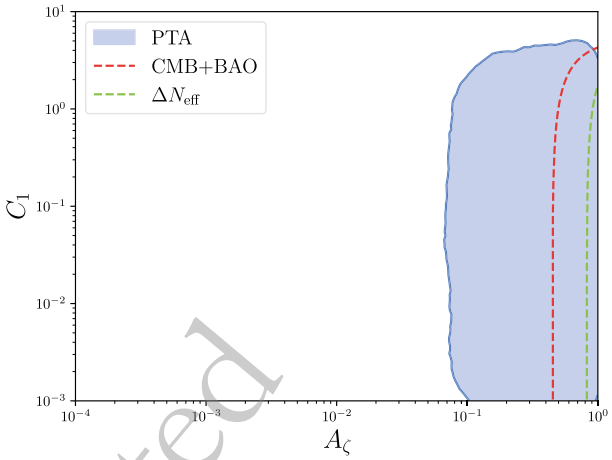

Fig. 7. (color online) The constraints on A_ζ and C_1 assuming $\sigma = 1$ and $C_2 = 0$. The blue shaded region represents the 95% credible intervals corresponding to the two-dimensional posterior distribution shown in Fig. 3 with the KDE method. The red and green lines denote the lower bounds of C_1 from CMB and BAO observations in Eq. (42) and $\Delta N_{\rm eff}$ in Eq. (41).

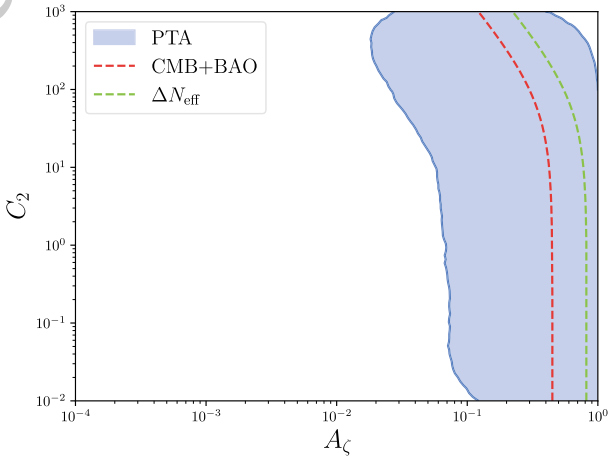

Fig. 8. (color online) The constraints on A_ζ and C_2 assuming $\sigma = 1$ and $C_1 = 0$. The blue shaded region represents the 95% credible intervals corresponding to the two-dimensional posterior distribution shown in Fig. 4 with the KDE method. The red and green lines denote the upper bounds of C_2 from CMB and BAO observations in Eq. (42) and $\Delta N_{\rm eff}$ in Eq. (41).

given by Eq. (41) and Eq. (42), respectively.

Furthermore, to better assess the plausibility of different models in explaining current PTA observations, we perform a detailed analysis of Bayes factors between different models. The Bayes factor is defined as $B_{i,j} = \frac{Z_i}{Z_j}$, where Z_i represents the evidence of model H_i. In addition to scalar-induced gravitational waves, we also investigate a hybrid model scenario where both SMBHBs and SIGWs contribute jointly. The energy density spectrum of SMBHBs is characterized by [7]

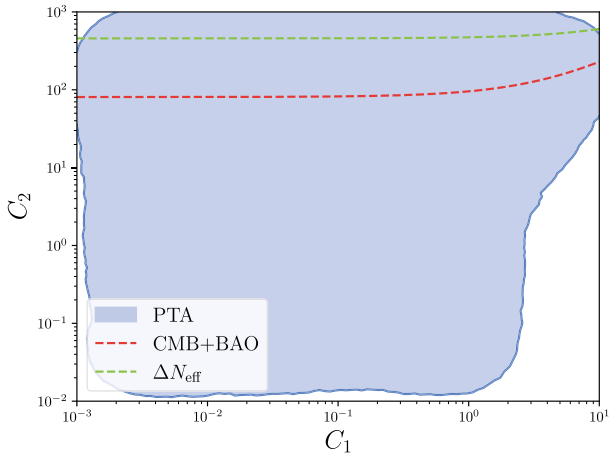

Fig. 9. (color online) The constraints on C_1 and C_2 assuming $\sigma = 1$ and $A_\zeta = 10^{-0.5}$. The blue shaded regions represent the 95% credible intervals corresponding to the two-dimensional posterior distribution shown in Fig. 5 with the KDE method. The black solid line and grey dashed line denote the upper bounds of C_2 from CMB and BAO observations in Eq. (42) and $\Delta N_{\rm eff}$ in Eq. (41).

$$\Omega_{\rm GW}^{\rm BH}(f) = \frac{2\pi^2 A_{\rm BHB}^2}{3H_0^2h^2}\left(\frac{f}{\rm year^{-1}}\right)^{5-\gamma_{\rm BHB}}{\rm year}^{-2}\,, \tag{43}$$

with the prior distribution for $\log_{10}A_{\rm BHB}$ assumed to follow a multivariate Gaussian distribution [7]

$$\begin{aligned}\boldsymbol{\mu}_{\rm BHB} &= \begin{pmatrix}-15.6\\ 4.7\end{pmatrix}\,,\\ \boldsymbol{\sigma}_{\rm BHB} &= 0.1\times\begin{pmatrix}2.8 & -0.026\\ -0.026 & 2.8\end{pmatrix}\,.\end{aligned} \tag{44}$$

As shown in Fig. 10, we calculated the Bayes factors between different models. The results indicate that when small-scale anisotropies in the primordial power spectrum are taken into account, the Bayesian factor for SIGWs within the considered parameter space is approximately 10. This suggests that, compared to the SMBHB model, SIGWs with different anisotropic parameters are more likely to dominate current PTA observations. To directly assess the statistical preference for small-scale anisotropy, the Bayes factor between the anisotropic models and the isotropic SIGW model ($C_1 = C_2 = 0$) can be derived simply by taking the ratio of the Bayes factors presented in Fig. 10. The Bayes factor for the most favored anisotropic case ($C_2 \neq 0$) relative to the isotropic case is approximately $\mathcal{B} \approx 14.31/13.24 \approx 1.08$, which is close to unity. This value indicates that current PTA data are insufficient to effectively distinguish between isotropic and anisotropic primordial power spectra on small scales.

B. Constraints from future observations and specific models

In Sec. IV A, we investigate the impact of second-order SIGWs, generated by small-scale anisotropic primordial power spectra, on current PTA observations. By combining PTA data with large-scale cosmological observations, we constrain the small-scale anisotropy parameters. Our results show that when considering a general parameterized form of the anisotropic primordial power spectrum, the presence of anisotropy parameters leads to a certain degree of degeneracy in the energy density spectrum of SIGWs. Consequently, current cosmological observations cannot impose stringent constraints on small-scale anisotropy parameters. To address this issue, we can combine SGWB observations at different frequency bands to jointly constrain or determine the parameter space of the small-scale primordial power spectrum.

As shown by the posterior distributions in Fig. 5, when second-order SIGWs dominate current PTA observations, the parameters A_ζ, σ, and f_* of the isotropic

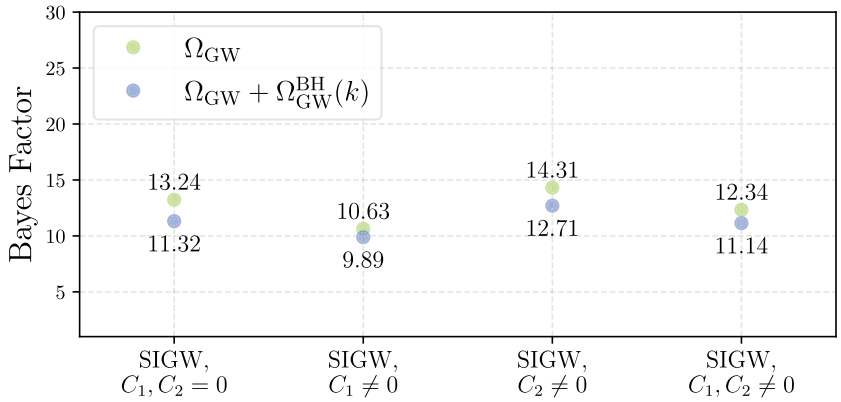

Fig. 10. (color online) The Bayes factors between different models. The vertical axis represents the Bayes factor of different models relative to SMBHB, and the horizontal axis represents the different models. The green dots are for models without SMBHB and the blue dots are for models in combination with the SMBHB signal.

primordial power spectrum $\mathcal{P}_{0,\zeta}$ can be constrained relatively effectively. However, the anisotropy parameters C_1 and C_2 remain unconstrained. In this analysis, we fix the isotropic parameters of $\mathcal{P}_{0,\zeta}$ to the median values determined by PTA observations in Fig. 5, and vary the anisotropy parameters C_1 and C_2 to examine their impact on SGWB observations in the LISA frequency band. More precisely, in order to explore the impact of anisotropic primordial power spectrum on the second-order SIGWs, we calculate the SNR ρ for LISA [68, 69]

$$\rho = \sqrt{T}\left[\int \mathrm{d}f \left(\frac{\bar{\Omega}_{\mathrm{GW},0}(f)}{\Omega_{\mathrm{n}}(f)}\right)^2\right]^{1/2}, \tag{45}$$

where T is the observation time and we set $T = 4$ years here. $\Omega_{\mathrm{n}}(f) = 2\pi^2 f^3 S_n/3H_0^2$, where H_0 is the Hubble constant, S_n is the strain noise power spectral density [69]. As illustrated in Fig. 5, if the second-order SIGWs generated by an anisotropic primordial power spectrum dominate the current PTA observations, then $f_* \approx 10^{-6.7}$ Hz, $A_\zeta \approx 10^{-0.6}$, and $\sigma \approx 1.2$. In Fig. 11, we present the signal-to-noise ratios of LISA corresponding to different anisotropy parameters C_1 and C_2 under this scenario. As shown in Fig. 11, the SNR of LISA increases with the peak position f_* of the primordial power spectrum. When the parameter $f_* > 10^{-3}$, the anisotropy parameters C_1 and C_2 have a significant impact on the SNR of LISA. Future observations of the SGWB in the LISA frequency band may thus provide a new window into studying anisotropic inflation models at small scales.

Furthermore, the gray region in Fig. 5 corresponds to the 1-σ range of the posterior of f_* when SIGWs dominate current PTA observations. When f_* lies within this gray region, regardless of the values of C_1 and C_2, the SNR of LISA does not exceed 10^{-2}. Therefore, the SIGWs generated by the primordial power spectrum under consideration cannot simultaneously dominate PTA observations and produce a significant impact on the SGWB in the LISA band. This behavior is markedly different from the SGWB produced by SMBHB. When the SMBHB model dominates the PTA signal, the corresponding energy density spectrum can still be detected by LISA [70]. Combining SGWB observations across different frequency bands to jointly constrain or determine various SGWB models and their corresponding parameter spaces may serve as an important tool in the future for distinguishing between different sources of the SGWB.

From the above discussion, we find that current cosmological observations are insufficient to place strong constraints on the small-scale anisotropic primordial power spectrum. More precise future observations, combined with SGWB measurements at other frequency bands, will be required to better constrain or determine the properties of the small-scale anisotropic primordial power spectrum. It should be noted that the small-scale anisotropic primordial power spectra considered here are given in parameterized form, in which the anisotropy parameter C_l is not subject to any restriction. However, in specific inflationary models, the anisotropy parameters are generally dictated by the intrinsic features of the model, so the parameter C_l is not completely free. As an illustration, Ref. [71] considered a system constructed by two scalar fields, specifically, an inflaton ϕ and a waterfall field χ, and a vector field $A_\mu(\mu = 0,1,2,3)$ which couples with the waterfall field. The corresponding action can be written as

$$\begin{aligned} S = &\frac{1}{2}\int \mathrm{d}^4x\sqrt{-g}R - \int \mathrm{d}^4x\sqrt{-g} \\ &\times\left[\frac{1}{2}g^{\mu\nu}\left(\partial_\mu\phi\partial_\nu\phi + \partial_\mu\chi\partial_\nu\chi\right) + V\left(\phi,\chi,A_\mu\right)\right] \\ &-\frac{1}{4}\int \mathrm{d}^4x\sqrt{-g}g^{\mu\nu}g^{\rho\sigma}f^2(\phi)F_{\mu\rho}F_{\nu\sigma}\,, \end{aligned} \tag{46}$$

where $F_{\mu\nu} \equiv \partial_\mu A_\nu - \partial_\nu A_\mu$ is the field strength of the vector field, and an arbitrary function $f(\phi)$ represents gauge

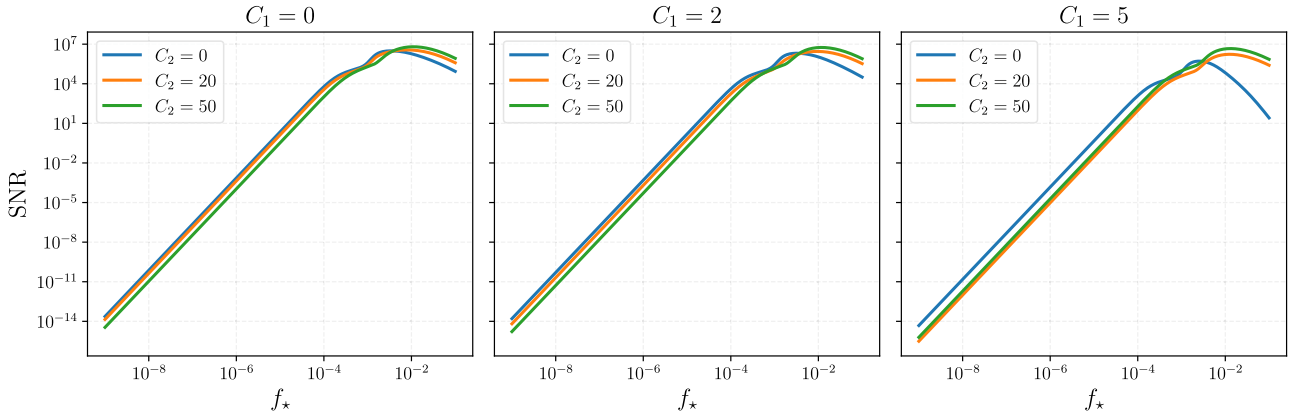

Fig. 11. (color online) The SNR of LISA as a function of f_* with different C_1 and C_2, calculated for fixed values of $A_\zeta = 10^{-0.6}$ and $\sigma = 1$. The gray bands represent the 1-σ range from the posterior of f_* shown in Fig. 5.

coupling. The potential of field $V(\phi,\chi,A_\mu)$ is given by

$$V(\phi,\chi,A^i)=\frac{\lambda}{4}\left(\chi^2-v^2\right)^2+\frac{1}{2}g^2\phi^2\chi^2+\frac{1}{2}m^2\phi^2+\frac{1}{2}h^2A^\mu A_\mu\chi^2\,. \tag{47}$$

In such a scenario, the anisotropic primordial power spectrum can be represented as

$$\mathcal{P}_\zeta^{\hat{\mathbf{n}}}(\mathbf{k})=\mathcal{P}_{0,\zeta}(k)\left(1-g_*\left(\hat{\mathbf{n}}\cdot\hat{\mathbf{k}}\right)^2\right)\,, \tag{48}$$

where

$$g_*=\frac{\beta}{1+\beta}\,,\ \beta\approx\frac{1}{f_e^2}\left(\frac{h^2|\mathbf{A}|}{g^2\phi_e}\right)^2\,. \tag{49}$$

In this model, g_* serves as the parameter quantifying anisotropy. When $\beta\gg1$, $g_*\approx1$, whereas when $\beta\ll1$, $g_*\approx\beta\ll1$. In this case, regardless of how the model parameters vary, it is impossible to generate a very large anisotropic primordial power spectrum. The above example illustrates that, in addition to the constraints from cosmological observations, specific anisotropic inflationary models may impose further restrictions on the anisotropy parameters. For a given model, current cosmological data can be combined with the properties of the model to jointly constrain the parameter space of the small-scale anisotropic primordial power spectrum.

V. CONCLUSION

In this study, we explored how small-scale anisotropic primordial power spectra affect the energy density spectrum of second-order SIGWs. In Sec. III, we derived the expression for the energy density spectrum of these waves under the influence of an anisotropic primordial power spectrum. This result is applicable to any form of small-scale anisotropic primordial power spectrum with $l\le4$ and remains independent of specific inflation models. As examples, we examined the gauge field inflation model and the Finslerian inflation model, which correspond to the primordial power spectra with $C_2\neq0$ and $C_1\neq0$, respectively. We investigated the impact of these two inflation models on current PTA observations and SNR of LISA, and extended the findings to a general scenario where both C_1 and C_2 are non-zero.

In Sec. IV, we discussed the constraints imposed by current PTA+CMB+BAO data on the small-scale anisotropic primordial power spectrum. Specifically, under the assumption that second-order SIGWs dominate current PTA observations, we analyzed the constraints imposed by PTA data on small-scale anisotropic inflation models. To better constrain the parameter space of different models, we incorporated large-scale cosmological observations and presented the resulting constraints on the parameter space of the small-scale anisotropic primordial power spectrum in Fig. 7–Fig. 9. In addition, we examined the feasibility that SIGWs generated by different small-scale anisotropic inflation models dominate current PTA signals. The results indicate that current cosmological data can only partially constrain the parameter space of these models, without definitively confirming or ruling them out.

Since current cosmological observations cannot effectively constrain the general form of the anisotropic primordial power spectrum, we have further considered the restrictions from future SGWB observations in the LISA frequency band, as well as from specific inflationary models. Using the isotropic primordial power spectrum parameters determined by PTA observations, we analyzed the impact of anisotropy parameters C_1 and C_2 on the SNR of LISA under the scenario where SIGWs dominate current PTA observations. The results show that the SIGWs generated by the primordial power spectrum under consideration cannot simultaneously dominate PTA observations and produce a significant impact on the SGWB in the LISA band. Furthermore, we briefly analyzed anisotropic primordial power spectra generated by specific models, noting that in certain anisotropic inflationary scenarios, the models themselves impose relatively strict constraints on the anisotropy parameters.

References

[1] G. Agazie *et al*. (NANOGrav), Astrophys. J. Lett. **951**, L8 (2023), arXiv: 2306.16213[astro-ph.HE].

[2] J. Antoniadis *et al*. (EPTA, InPTA:), Astron. Astrophys. **678**, A50 (2023), arXiv: 2306.16214[astro-ph.HE].

[3] D. J. Reardon *et al*., Astrophys. J. Lett. **951**, L6 (2023), arXiv: 2306.16215[astro-ph.HE]

[4] H. Xu *et al*., Res. Astron. Astrophys. **23**, 075024 (2023), arXiv: 2306.16216[astro-ph.HE]

[5] Z.-Q. Shen, G.-W. Yuan, Y.-Y. Wang, and Y.-Z. Wang, (2023), arXiv: 2306.17143[astro-ph.HE].

[6] J. Ellis, M. Fairbairn, G. Hütsi, J. Raidal, J. Urrutia, V. Vaskonen, and H. Veermäe, Phys. Rev. D **109**, L021302 (2024), arXiv: 2306.17021[astro-ph.CO]

[7] A. Afzal *et al*. (NANOGrav), Astrophys. J. Lett. **951**, L11 (2023), arXiv: 2306.16219[astro-ph.HE].

[8] J. Ellis, M. Lewicki, C. Lin, and V. Vaskonen, (2023), arXiv: 2306.17147[astro-ph.CO].

[9] N. Kitajima, J. Lee, K. Murai, F. Takahashi, and W. Yin, (2023), arXiv: 2306.17146[hep-ph].

[10] Y. Bai, T.-K. Chen, and M. Korwar, (2023), arXiv: 2306.17160[hep-ph].

[11] K. Fujikura, S. Girmohanta, Y. Nakai, and M. Suzuki, (2023), arXiv: 2306.17086[hep-ph].

[12] T. Bringmann, P. F. Depta, T. Konstandin, K. Schmidt-

Hoberg, and C. Tasillo, (2023), arXiv: 2306.09411 [astro-ph.CO].
[13] K. N. Ananda, C. Clarkson, and D. Wands, Phys. Rev. D **75**, 123518 (2007), arXiv: gr-qc/0612013
[14] Z. Chang, Y.-T. Kuang, D. Wu, and J.-Z. Zhou, JCAP **2024**, 044 (2024), arXiv: 2312.14409[astro-ph.CO]
[15] S. Balaji, G. Domènech, and G. Franciolini, (2023), arXiv: 2307.08552[gr-qc].
[16] Y.-F. Cai, X.-C. He, X. Ma, S.-F. Yan, and G.-W. Yuan, (2023), arXiv: 2306.17822[gr-qc].
[17] Q.-H. Zhu, Z.-C. Zhao, and S. Wang, "Joint implications of bbn, cmb, and pta datasets for scalar-induced gravitational waves of second and third orders," (2023), arXiv: 2307.03095[astro-ph.CO].
[18] S. Wang, Z.-C. Zhao, J.-P. Li, and Q.-H. Zhu, "Exploring the implications of 2023 pulsar timing array datasets for scalar-induced gravitational waves and primordial black holes," (2023), arXiv: 2307.00572[astro-ph.CO].
[19] J.-Z. Zhou, X. Zhang, Q.-H. Zhu, and Z. Chang, JCAP **05**, 013 (2022), arXiv: 2106.01641[astro-ph.CO]
[20] N. Aghanim *et al*. (Planck), Astron. Astrophys. **641**, A6 (2020), [Erratum: Astron.Astrophys. 652, C4 (2021)], arXiv: 1807.06209[astro-ph.CO].
[21] T. Bringmann, P. Scott, and Y. Akrami, Phys. Rev. D **85**, 125027 (2012), arXiv: 1110.2484[astro-ph.CO]
[22] L. Liu, Z.-C. Chen, and Q.-G. Huang, Phys. Rev. D **109**, L061301 (2024), arXiv: 2307.01102[astro-ph.CO]
[23] S. Wang, Z.-C. Zhao, J.-P. Li, and Q.-H. Zhu, Phys. Rev. Res. **6**, L012060 (2024), arXiv: 2307.00572[astro-ph.CO]
[24] G. Franciolini, A. Iovino, Junior., V. Vaskonen, and H. Veermae, Phys. Rev. Lett. **131**, 201401 (2023), arXiv: 2306.17149[astro-ph.CO]
[25] J.-P. Li, S. Wang, Z.-C. Zhao, and K. Kohri, JCAP **05**, 109 (2024), arXiv: 2403.00238[astro-ph.CO]
[26] L. Liu, Z.-C. Chen, and Q.-G. Huang, JCAP **11**, 071 (2023), arXiv: 2307.14911[astro-ph.CO]
[27] Q.-H. Zhu, Z.-C. Zhao, S. Wang, and X. Zhang, Chin. Phys. C **48**, 125105 (2024), arXiv: 2307.13574[astro-ph.CO]
[28] G. Domènech, S. Pi, A. Wang, and J. Wang, JCAP **08**, 054 (2024), arXiv: 2402.18965[astro-ph.CO]
[29] N. Bartolo, D. Bertacca, V. D. Luca, G. Franciolini, S. Matarrese, M. Peloso, A. Ricciardone, A. Riotto, and G. Tasinato, Journal of Cosmology and Astroparticle Physics **2020**, 028 (2020)
[30] J.-P. Li, S. Wang, Z.-C. Zhao, and K. Kohri, "Primordial non-gaussianity and anisotropies in gravitational waves induced by scalar perturbations," (2023), arXiv: 2305.19950[astro-ph.CO].
[31] L. Ackerman, S. M. Carroll, and M. B. Wise, Phys. Rev. D **75**, 083502 (2007), [Erratum: Phys.Rev.D 80, 069901 (2009)], arXiv: astro-ph/0701357.
[32] J. Soda, Classical and Quantum Gravity **29**, 083001 (2012)
[33] A. Maleknejad, M. Sheikh-Jabbari, and J. Soda, Physics Reports **528**, 161 (2013)
[34] E. Dimastrogiovanni, N. Bartolo, S. Matarrese, and A. Riotto, Advances in Astronomy 2010, 1 (2010).
[35] C. Chen and A. Ota, Physical Review D **106** (2022), 10.1103/physrevd.106.063507.
[36] C. Pfeifer and M. N. R. Wohlfarth, Physical Review D **85** (2012), 10.1103/physrevd.85.064009.
[37] X. Li and Z. Chang, Physical Review D **90** (2014), 10.1103/physrevd.90.064049.
[38] N. Russell, Physical Review D **91** (2015), 10.1103/physrevd.91.045008.
[39] Z. Chang, P. K. Rath, Y. Sang, D. Zhao, and Y. Zhou, Mon. Not. Roy. Astron. Soc. **479**, 1327 (2018), arXiv: 1806.11425[astro-ph.CO]
[40] B. A. Bassett, S. Tsujikawa, and D. Wands, Rev. Mod. Phys. **78**, 537 (2006), arXiv: astro-ph/0507632
[41] Y.-F. Cai, C. Lin, B. Wang, and S.-F. Yan, Phys. Rev. Lett. **126**, 071303 (2021), arXiv: 2009.09833[gr-qc]
[42] M. A. Gorji and M. Sasaki, Phys. Lett. B **846**, 138236 (2023), arXiv: 2302.14080[gr-qc]
[43] V. K. Oikonomou, Phys. Rev. D **108**, 043516 (2023), arXiv: 2306.17351[astro-ph.CO]
[44] Z. Chang, X. Zhang, and J.-Z. Zhou, Phys. Rev. D **107**, 063510 (2023), arXiv: 2209.07693[astro-ph.CO]
[45] K. Inomata, JCAP **03**, 013 (2021), arXiv: 2008.12300[gr-qc]
[46] K. Kohri and T. Terada, Phys. Rev. D **97**, 123532 (2018), arXiv: 1804.08577[gr-qc]
[47] C. Yuan and Q.-G. Huang, iScience **24**, 102860 (2021), arXiv: 2103.04739[astro-ph.GA]
[48] A. Maleknejad and M. M. Sheikh-Jabbari, Phys. Rev. D **85**, 123508 (2012), arXiv: 1203.0219[hep-th]
[49] C. Chen and A. Ota, Phys. Rev. D **106**, 063507 (2022), arXiv: 2205.07810[astro-ph.CO]
[50] Z. Zhou, J. Jiang, Y.-F. Cai, M. Sasaki, and S. Pi, Phys. Rev. D **102**, 103527 (2020), arXiv: 2010.03537[astroph.CO]
[51] A. Addazi, S. Capozziello, and Q. Gan, JCAP **08**, 051 (2022), arXiv: 2204.07668[astro-ph.CO]
[52] Z.-Z. Peng, C. Fu, J. Liu, Z.-K. Guo, and R.-G. Cai, JCAP **10**, 050 (2021), arXiv: 2106.11816[astro-ph.CO]
[53] L.-Y. Chen, H. Yu, and P. Wu, Phys. Lett. B **849**, 138457 (2024), arXiv: 2401.07523[gr-qc]
[54] S. Wang, T. Terada, and K. Kohri, Phys. Rev. D **99**, 103531 (2019), [Erratum: Phys.Rev.D 101, 069901 (2020)], arXiv:1903.05924[astro-ph.CO].
[55] K. Saikawa and S. Shirai, JCAP **05**, 035 (2018), arXiv: 1803.01038[hep-ph]
[56] A. Maleknejad, M. M. Sheikh-Jabbari, and J. Soda, Phys. Rept. **528**, 161 (2013), arXiv: 1212.2921[hep-th]
[57] X. Li, S. Wang, and Z. Chang, Eur. Phys. J. C **75**, 260 (2015), arXiv: 1502.02256[gr-qc]
[58] W. G. Lamb, S. R. Taylor, and R. van Haasteren, Phys. Rev. D **108**, 103019 (2023), arXiv: 2303.15442[astroph.HE]
[59] C. J. Moore and A. Vecchio, Nature Astron. **5**, 1268 (2021), arXiv: 2104.15130[astro-ph.CO]
[60] A. Mitridate, D. Wright, R. von Eckardstein, T. Schröder, J. Nay, K. Olum, K. Schmitz, and T. Trickle, (2023), arXiv: 2306.16377[hep-ph].
[61] T. N. Collaboration, "Kde representations of the gravitational wave background free spectra present in the nanograv 15-year dataset," (2023).
[62] G. Ashton *et al*., Astrophys. J. Suppl. **241**, 27 (2019), arXiv: 1811.02042[astro-ph.IM]
[63] J. S. Speagle, Mon. Not. Roy. Astron. Soc. **493**, 3132 (2020), arXiv: 1904.02180[astro-ph.IM]
[64] S. Koposov, J. Speagle, K. Barbary, G. Ashton, E. Bennett, J. Buchner, C. Scheffler, B. Cook, C. Talbot, J. Guillochon, P. Cubillos, A. A. Ramos, M. Dartiailh, Ilya, E. Tollerud, D. Lang, B. Johnson, jtmendel, E. Higson, T. Vandal, T. Daylan, R. Angus, patelR, P. Cargile, P. Sheehan, M. Pitkin, M. Kirk, J. Leja, joezuntz, and D. Goldstein,

"joshspeagle/dynesty: v2.1.4," (2024).
[65] I. Ben-Dayan, B. Keating, D. Leon, and I. Wolfson, JCAP **06**, 007 (2019), arXiv: 1903.11843[astro-ph.CO]
[66] J. Cang, Y.-Z. Ma, and Y. Gao, Astrophys. J. **949**, 64 (2023), arXiv: 2210.03476[astro-ph.CO]
[67] T. J. Clarke, E. J. Copeland, and A. Moss, JCAP **10**, 002 (2020), arXiv: 2004.11396[astro-ph.CO]
[68] X. Siemens, J. Ellis, F. Jenet, and J. D. Romano, Class. Quant. Grav. **30**, 224015 (2013), arXiv: 1305.3196[astro-ph.IM]
[69] T. Robson, N. J. Cornish, and C. Liu, Class. Quant. Grav. **36**, 105011 (2019), arXiv: 1803.01944[astro-ph.HE]
[70] J. Ellis, M. Fairbairn, G. Franciolini, G. Hütsi, A. Iovino, M. Lewicki, M. Raidal, J. Urrutia, V. Vaskonen, and H. Veermäe, Phys. Rev. D **109**, 023522 (2024), arXiv: 2308.08546[astro-ph.CO]
[71] S. Yokoyama and J. Soda, JCAP **08**, 005 (2008), arXiv: 0805.4265[astro-ph]